First-principles study of migration mechanisms and diffusion of oxygen in zinc oxide

Paul Erhart and Karsten Albe
Institut für Materialwissenschaft, Technische Universität Darmstadt, Petersenstraße 23, D-64287 Darmstadt, Germany
(Received 7 December 2005; revised manuscript received 6 February 2006; published 22 March 2006)

We have performed density-functional theory calculations in conjunction with the climbing image nudged elastic band method in order to study the self-diffusion of oxygen in zinc oxide. To this end, we have derived the complete set of migration paths for vacancies as well as interstitials in wurtzite crystals and deduced expressions which provide the link to experimentally accessible tracer diffusion coefficients. The calculated migration barriers are consistent with annealing experiments on irradiated samples. We find that vacancy and interstitialcy mechanisms dominate under zinc and oxygen-rich conditions, respectively. This refutes the belief that vacancy mechanisms can be operational in experiments in oxygen-rich atmosphere. Our results provide the basis for the (re-)interpretation of diffusion experiments, and pave the way towards the development of reliable continuum models for device simulation.

DOI: 10.1103/PhysRevB.73.115207 PACS number(s): 61.72.Bb, 61.72.Ji, 66.30.Dn, 71.55.Gs

I. INTRODUCTION

Zinc oxide is widely used in electronic as well as optoelectronic devices and also of fundamental interest as a prototypical oxide material.[1] Since its properties are highly sensitive to the nature and concentrations of lattice imperfections, defects in ZnO have been intensively investigated in the past. Despite these efforts, the current understanding of the thermodynamics and kinetics of point defects is still incomplete.

The mobilities of intrinsic point defects determine the annealing behavior of materials. Moreover, diffusion pertains to the degradation of ZnO varistors, which is believed to occur via the migration of interstitials to grain boundary regions.[2] Furthermore, the annealing of defects by rapid defect migration is likely to contribute to the remarkable radiation hardness of zinc oxide.[3] Knowledge of diffusivities and diffusion mechanisms is obviously instrumental in order to obtain a fundamental understanding of these processes, to devise strategies for controlling the migration of certain species, and to develop continuum models for device simulation.

Diffusion experiments provide information on atomic migration and in addition allow one to gain insights into the defect chemistry in general.[4] The interpretation of diffusion experiments is, however, often difficult and evidence for defect properties is indirect. In the past several experimental studies have been concerned with the determination of self-diffusion coefficients,[5–10] but the data scatter is large and no consensus on activation energies, exponential prefactors, or migration mechanisms has been achieved. Therefore, a systematic theoretical investigation is highly desirable in order to obtain more fundamental insights on the subject. Hitherto, theoretical investigations based on quantum-mechanical calculations have been conducted to explore static properties of intrinsic as well as extrinsic point defects in zinc oxide (see, e.g., Refs. 11–18). Recently, migration barriers were calculated for Li in wurtzitic ZnO (Ref. 18) and for the doubly positively charged zinc interstitial in cubic ZnO (zinc blende structure)[19] but at present there is no comprehensive study on the mobilities of intrinsic point defects in zinc oxide.

In order to determine migration paths and barriers for vacancy and interstitial motion in zinc oxide, we have performed density-functional theory (DFT) calculations in conjunction with the climbing image (CI) nudged elastic band method (NEB).[20,21] The complete set of migration paths to first and second nearest neighbors on the respective sublattice has been derived for the wurtzite lattice taking into account the non-ideal axial ratio of ZnO as well as defect induced symmetry breaking. By using the CI-NEB method, a minimal number of constraints was imposed when searching for saddle points. Unlike experiments which provide only a compound value for the diffusivity, the present approach allows to separate unequivocally the various contributions. Since we consider isolated intrinsic point defects only, association of defects, in particular with impurities,[14,18,22] is not included in the present study.

The paper is organized as follows. In the following section, we summarize the equations describing diffusion in terms of attempt frequencies and migration barriers. In Sec. III we describe the computational framework and discuss potential sources of errors. The migration paths and associated migration barriers are presented in Sec. IV and subsequently used to derive diffusivities in Sec. V. The paper is concluded in Sec. VI.

II. BACKGROUND

The rate at which a single isolated point defect d moves via migration path i can usually be described by an Arrhenius law[4]

$$\Gamma_i^d = \Gamma_{0,i}\exp[-\Delta G_i^m/k_B T]. \quad (1)$$

In principle, the attempt frequency $\Gamma_{0,i}$ can be obtained within harmonic transition-state theory via the Vineyard equation,[23] but it is frequently approximated by a characteristic frequency such as the lowest Raman mode[8] or the Einstein or Debye frequency. The free enthalpy of migration ΔG_i^m is given by

$$\Delta G_i^m = \Delta H_i^m + p\Delta V_i^m - T\Delta S_i^m, \quad (2)$$

where ΔH_i^m is the enthalpy of migration, ΔV_i^m is the migration volume, and ΔS_i^m denotes the migration entropy. For

small pressures, the pressure-volume term approaches zero, and can be disregarded. The entropy term enters the prefactor but since migration entropies are usually in the range of 1 to $2k_B$, this constitutes merely a minor effect.[24,25] The factor which most crucially affects the jump rate (and eventually the diffusion rate) is the migration enthalpy ΔH_i^m. Its determination for different defects, migration paths, and charge states is the core subject of the present work.

III. DETAILS OF THE CALCULATIONS

A. Computational method

Calculations within density-functional theory were carried out with the vienna *ab initio* simulation package[26] (VASP) using the projector augmented wave (PAW) method[27] and the generalized gradient approximation (GGA) in the parametrization by Perdew and Wang (PW91).[28] In order to properly account for the position of the Zn-3*d* levels the GGA+U scheme in the formulation by Dudarev *et al.*[29] was adopted as described in detail in Ref. 30. We employed hexagonal 32-atom supercells equivalent to $2\times2\times2$ primitive unit cells. The plane-wave energy cutoff was set to 500 eV and a Γ-point centered $2\times2\times2$ k-point grid was used for Brillouin zone sampling.

For the crystallographic parameters of w-ZnO we obtained $a=3.196$ Å, $c/a=1.606$, and $u=0.381$ which compare well with the experimental values $a=3.242$ Å, $c/a=1.600$, and $u=0.382$. From fitting the energy-volume data to the Birch-Murnaghan equation of state[31] a bulk modulus of 136 GPa was determined in good agreement with experimental data.[32] Also the calculated formation enthalpy of $\Delta H_f=-3.46$ eV/f.u. agrees very well with the experimental value of $\Delta H_f=-3.58$ eV/f.u. The bandgap at the Γ point is 1.83 eV which underestimates the experimental value of $\sim$3.4 eV but is consistent with previous DFT calculations.[15,16]

B. Determination of diffusion paths

The wurtzite lattice is composed of two interpenetrating hexagonal close packed (hcp) lattices being exclusively occupied by zinc and oxygen atoms, respectively. It follows that the diffusion paths for oxygen vacancies (V_O) can be deduced from the diffusion paths available on the hcp lattice; the same applies for oxygen interstitials (O_i) which adopt dumbbell-like ground state configurations.[14,17] Since antisites have extremely high formation energies,[11–13] antisite mediated diffusion mechanisms can be excluded.

In order to obtain the energy barriers for the various diffusion paths we employed the climbing image nudged elastic band method[20,21] as implemented in VASP by Henkelman, Jónsson, and others.[33] We checked the convergence of the minimum energy path (MEP) and the saddle point by using up to eight images. As the saddle point determination worked reliably for a small number of images, only three or four images were used for most computations. The images of the NEB were relaxed until the maximum residual force was less than 15 meV/Å. For several configurations we checked the saddle points by performing dimer calculations[34] at a higher level of convergence. The differences between the CI-NEB and the dimer saddle point energies amounted to about 1 meV and less, which confirms the reliability of the CI-NEB approach. Since the defect charge states vary with the electron chemical potential due to the explicit Fermi energy dependence of the formation enthalpies, migration barriers were determined for all relevant charge states (V_O: $0\leqslant q\leqslant+2$; O_i: $-2\leqslant q\leqslant+2$).

C. Potential sources of error

In DFT calculations of point defect properties, three major sources of error have to be taken into account:[30] (1) the underestimation of the bandgap, (2) elastic, and, if charge defects are considered, (3) electrostatic image interactions. The underestimation of the bandgap is an intrinsic shortcoming of the local density (LDA) and generalized gradient (GGA) approximations. It is crucial to correct for this deficiency if formation enthalpies (ΔH^f) are to be computed for configurations with different electronic properties, for example, acceptorlike and donorlike defects.[12,35] On the other hand, migration barriers (ΔH^m) are obtained as energy *differences* between *electronically similar* configurations. In addition, unlike formation enthalpies, they do not depend explicitly on the Fermi level. In the present work the GGA+U method is used to correct for the position of the Zn-3*d* levels which also results in a significantly larger bandgap (1.83 eV with GGA+U vs 0.75 eV with "standard" GGA). The migration enthalpies for the lowest energy paths obtained with GGA and GGA+U differ by at most 0.3 eV which amounts to a much smaller effect than in the case of formation enthalpies.[30] Therefore, the remaining bandgap error should have a small impact on the calculated migration barriers.

Due to the use of periodic boundary conditions, strain and electrostatic interactions are present between defects in neighboring supercells: Strain interactions scale approximately as $O(V^{-1/3})$ (where V is the supercell volume). If calculations are performed at fixed lattice constants, the $p\Delta V_f$ term (where p is the pressure and ΔV_f is the defect formation volume) is nonzero and leads to an additional contribution to the calculated formation enthalpy. For charged defects image charge interactions are present, which can be corrected based on a multipole expansion of the excess charge distribution.[36] Again, these effects are crucial if formation enthalpies are going to be compared. In contrast, in the case of migration barriers, the initial and transition states are structurally as well as electronically similar, and migration volumina are typically just about one tenth of the respective defect formation volumina. Therefore, finite size effects can be expected to play a minor role in the calculation of migration barriers.

From this argumentation we conclude that the errors in the migration barriers are expected to be smaller than the errors in the formation enthalpies. Since the typical error in the formation enthalpies is estimated[11–13,17] to be smaller than 0.1 eV, the error in the migration barriers should be some fraction of this value.

As will be shown below, the activation energy observed in tracer experiments, comprises both the migration as well as

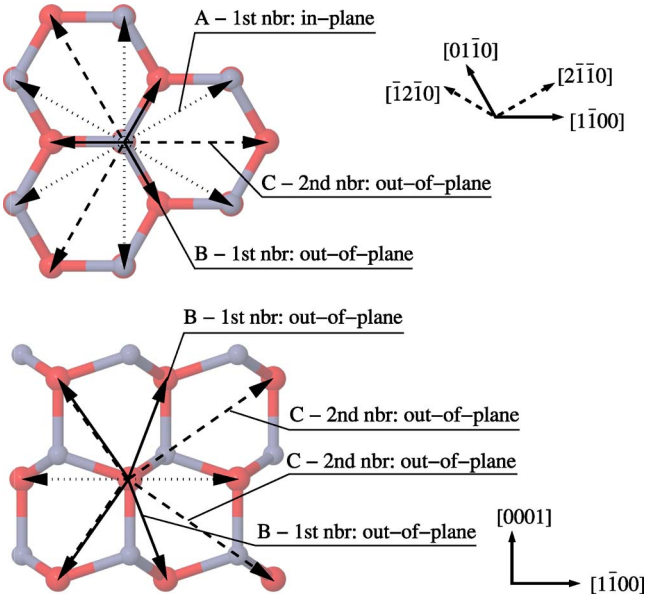

FIG. 1. (Color online) Diffusion paths accessible to oxygen vacancies on the wurtzite lattice via jumps to first or second nearest oxygen sites. Projections along [0001] (top) and [11$\bar{2}$0] (bottom).

the formation enthalpy [see Eqs. (4) and (5) below]. The relative error in the tracer diffusivity is, therefore, not governed by the error in ΔH^m but by the error in ΔH^f.

IV. MIGRATION PATHS

A. Vacancy diffusion

The possible diffusion paths via first as well as second nearest oxygen neighbors are schematically shown in Fig. 1. Among the jumps to first nearest oxygen sites, there are six symmetry equivalent paths in the (0001) plane (A, 1st nbr.: in-plane) and six equivalent paths with components parallel to the [0001] axis (B, 1st nbr.: out-of-plane). On an ideal hcp lattice ($c/a=\sqrt{8/3}=1.633$) these two paths are equivalent. In the present case they are, however, distinct, since the axial ratio of the oxygen hcp lattice is slightly smaller than ideal ($c/a=1.606$). Considering jumps to second nearest oxygen sites, we find another six symmetry equivalent possibilities for upward and downward motion (C, 2nd nbr.: out-of-plane). Both out-of-plane paths also lead to in-plane displacements of the migrating atom.

The calculated diffusion barriers are compiled in Table I. The migration enthalpies for first nearest neighbor migration display a rather diverse behavior. In the neutral charge state the in-plane migration barrier is 0.7 eV lower than its out-of-plane counterpart indicating anisotropic diffusion behavior. On the other hand, for the +2 charge state process B possesses the lowest barrier and the diffusivity should display isotropic behavior. The charge state +1 represents an intermediate case.

B. Interstitial diffusion

There are at least three interstitial configurations which have been identified as local minima of the energy hypersurface based on DFT calculations.[17] In equilibrium oxygen interstitials adopt the dumbbell ($O_{i,\mathrm{db}}$) or the rotated dumbbell ($O_{i,\mathrm{db\text{-}rot}}$) configuration. The highly symmetric octahedral interstitial ($O_{i,\mathrm{oct}}$) is energetically unfavorable as a ground state configuration, but it can occur as an intermediate state along the diffusion path as will be discussed below.

TABLE I. Energy barriers for vacancy and interstitial mediated migration of oxygen in units of eV as obtained from CI-NEB calculations. The formation enthalpies of the respective ground state configurations obtained in Ref. 30 are included for reference (zinc-rich conditions, Fermi level at valence band maximum). See Figs. 1 and 2 for definition of migration paths.

Migration path			Charge state				
			$q=+2$	$q=+1$	$q=0$	$q=-1$	$q=-2$
		Oxygen vacancy V_O					
1st nbr.: in-plane	A		1.49	1.37	1.87		
1st nbr.: out-of-plane	B		1.09	1.38	2.55		
2nd nbr.: out-of-plane	C		3.62	3.79	4.29		
formation enthalpy			–0.73	0.71	1.71		
		Oxygen interstitial O_i					
1st nbr.: in-plane	A_1	$O_{i,\mathrm{db}} \leftrightarrow O_{i,\mathrm{db}}$	1.34	1.25	1.09		
1st nbr.: in-plane	A_2	$O_{i,\mathrm{db\text{-}rot}} \leftrightarrow O_{i,\mathrm{db\text{-}rot}}$	1.03	0.98	0.95	0.23	0.40
1st nbr.: out-of-plane	B_1	$O_{i,\mathrm{db}} \leftrightarrow O_{i,\mathrm{db\text{-}rot}}$	1.23	1.09	0.81	0.43	0.88
1st nbr.: out-of-plane	B_2	$O_{i,\mathrm{db}} \leftrightarrow O_{i,\mathrm{db\text{-}rot}}$	1.23	1.09	0.81	0.43	0.88
2nd nbr.: out-of-plane	C	$O_{i,\mathrm{db}} \leftrightarrow O_{i,\mathrm{db\text{-}rot}}$	1.98	1.78	1.60	0.60	1.37
ground state (g.s.)				$O_{i,\mathrm{db}}$		$O_{i,\mathrm{db\text{-}rot}}$	
formation enthalpy			5.08	4.59	4.70	7.08	8.79
energy difference		g.s. $\rightarrow O_{i,\mathrm{db}}/O_{i,\mathrm{db\text{-}rot}}$	+0.31	+0.27	+0.13	+0.43	+0.88
energy difference		g.s. $\rightarrow O_{i,\mathrm{oct}}$	+1.80	+1.73	+1.53	+0.21	+0.48

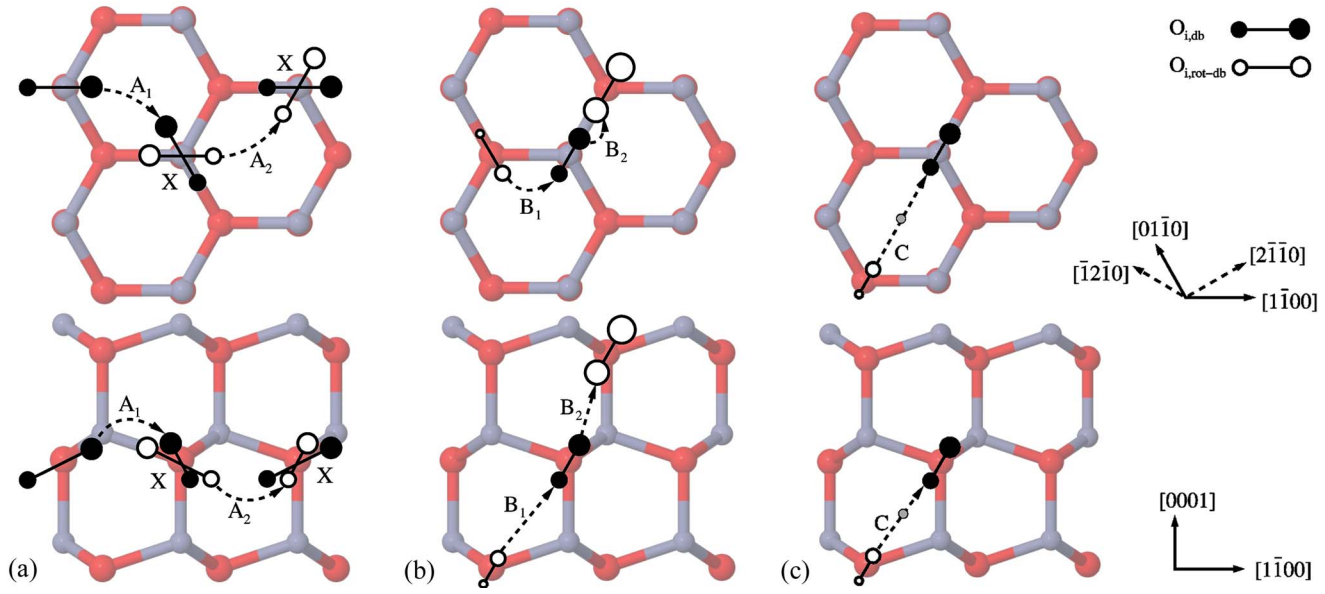

FIG. 2. (Color online) Diffusion paths accessible to oxygen interstitials on the wurtzite lattice via jumps to first or second nearest neighbor sites. Panels (a) and (b) show in-plane and out-of-plane diffusion paths to first nearest oxygen neighbors, panel (c) illustrates out-of-plane diffusion via second nearest oxygen neighbors. The size of the spheres scales with the position of the atom along the [0001] axis.

The two dumbbell configurations ($O_{i,db}$ and $O_{i,db\text{-}rot}$) possess a threefold symmetry axis, i.e., rotations about the [0001]-axis by multiples of 120° generate symmetry equivalent copies of the original defect. Furthermore (ignoring small differences in the atomic relaxations), the $O_{i,db}$ and $O_{i,db\text{-}rot}$ can be transformed into each other by application of a sixfold mirror axis (6_m). In the following, we refer to this "on-site" transformation as process *X*.

While in neutral and positive charge states the two oxygen atoms are bonded, they adopt a "split-interstitial" configuration in negative charge states.[17] In spite of this difference, the migration paths can be described on a similar basis for all charge states. Invoking the symmetry of the lattice the following mechanisms for oxygen interstitial migration can be distinguished, which are illustrated in detail in Figs. 2(a)–2(c).

(a) *In-plane movement*: *Processes* A_1 *and* A_2. In process A_1 one of the atoms of a dumbbell interstitial ($O_{i,db}$) moves away from its partner and forms a new dumbbell with one of the two next nearest oxygen atoms. Due to the threefold symmetry axis of the dumbbell there are three dumbbell orientations per oxygen site with two possible "target" atoms each, such that all of the six nearest in-plane neighbors on the hcp oxygen lattice can be reached. Process A_2 is the equivalent migration path for a rotated dumbbell interstitial.

(b) *Out-of-plane movement*: *Processes* B_1 *and* B_2. In both processes one of the atoms in the dumbbell (rotated dumbbell) moves to one of the first nearest out-of-plane neighbors forming a rotated dumbbell (dumbbell) interstitial at the new site.

(c) *Out-of-plane movement*: *Process* C. This process is similar to processes B_1 and B_2, but the interstitial migrates via jumps to second nearest oxygen neighbors thereby bridging larger distances in the lattice. The moving atom traverses through the octahedral interstitial configuration as indicated in Fig. 2(c) by the small grey spheres.

Equivalent to process B for vacancy migration, all of the out-of-plane migration paths (processes B_1, B_2, C) involve in-plane displacements as well. The concatenation of these processes leads to the migration of oxygen via an interstitialcy mechanism.

For the on-site transformation (process *X*), activation energies smaller than 0.1 eV are obtained (with respect to the configuration which is higher in energy). Since all other energy barriers in the system are at least by a factor of two larger (compare Table I), this process should never be rate determining and is not considered further. The energy barriers for the remaining migration processes are compiled in Table I. For the (out-of-plane) processes B_1, B_2, and C, which implicitly transform between the two dumbbell states, only the barrier from the respective ground state configuration is given ($O_{i,db}$ for $q=0,+1,+2$ and $O_{i,db\text{-}rot}$ for $q=-1$, -2).

As shown in Fig. 3, all processes show comparable trends with charge state. Going from charge state +2 to charge state 0 the barriers decrease slightly. A sudden drop occurs as the charge state becomes negative but the barriers rise again as yet another electron is added to the system ($q=-2$). For all paths the barriers are minimal for a charge state of −1.

The significantly lower migration barriers for oxygen interstitial migration in negative charge states can be rationalized based on the analysis of oxygen interstitial configurations given in Ref. 17. In neutral and positive charge states, the ground state configuration is stabilized by the formation of a strong oxygen-oxygen bond. When the system is negatively charged, it is favorable to split this bond and to adopt a configuration in which the oxygen atoms are relatively far apart. Migration of oxygen interstitials in neutral or positive

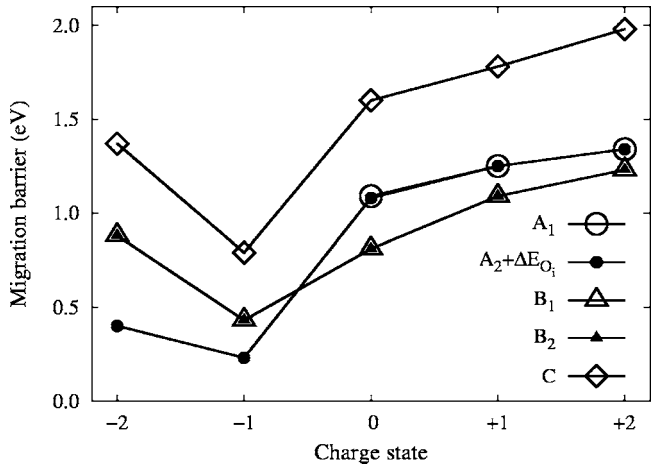

FIG. 3. Charge state dependence of oxygen interstitial migration enthalpies. For the in-plane path A_2, the energy difference (ΔE_{O_i}) between the dumbbell ($O_{i,db}$) and rotated dumbbell ($O_{i,db\text{-}rot}$) configurations has been included.

charge states thus requires breaking the strong oxygen-oxygen bond. On the other hand, for negative charge states motion of oxygen interstitials can be accomplished by breaking and reforming a minimal set of bonds leading to significantly lower migration barriers.

The energy surface for oxygen interstitial migration possesses many local minima ($O_{i,db}$, $O_{i,db\text{-}rot}$, $O_{i,oct}$) and saddle points, and is also quite flat in some regions (compare, e.g., the "on-site" transformation process *X*). As a result, the minimum energy paths are rather complex, which is schematically depicted in Fig. 4 for the charge states $q=+2$, 0, and -2.

The in-plane migration paths A_1 and A_2 possess simple saddle points. For the neutral and positive charge states, they are almost identical if the energy difference between the dumbbell ($O_{i,db}$) and rotated dumbbell ($O_{i,db\text{-}rot}$) is taken into account (compare Fig. 3). The saddle point is close in energy to the octahedral interstitial which is plausible considering Fig. 2(a). For the negative charge states, the migration barrier A_2 is very low and the saddle point configuration is again very close to the octahedral interstitial configuration ($O_{i,oct}$). Since the energy barrier for process A_2 is lower than the energy difference between $O_{i,db\text{-}rot}$ and $O_{i,db}$, the path A_1 becomes redundant.

The out-of-plane paths B_1 and B_2 yield practically identical saddle points. For the negative charge states we find that the saddle point for the transformation of $O_{i,db\text{-}rot}$ into $O_{i,db}$ almost coincides with the (regular) dumbbell ($O_{i,db}$) configuration. Thus, the barrier for the migration of $O_{i,db\text{-}rot}$ is essentially given by the energy difference between $O_{i,db\text{-}rot}$ and $O_{i,db}$.

The most complex minimum energy path is observed for the migration along path C. For all charge states the octahedral interstitial occurs as an intermediate state as indicated in Fig. 2. While the charge state is changing from +2 to −2 the depth of the local minimum associated with the octahedral interstitial changes from 0.18 eV ($q=+2$) to 0.89 eV ($q=-2$). At the same time the local minimum corresponding to the rotated dumbbell ($q\geq 0$) and dumbbell ($q<0$) states, respectively, becomes more and more shallow. In order to deal with these features of the energy surface properly, one would need to describe the migration process C in negative charge states similar to a reaction with preequilibrium. However,

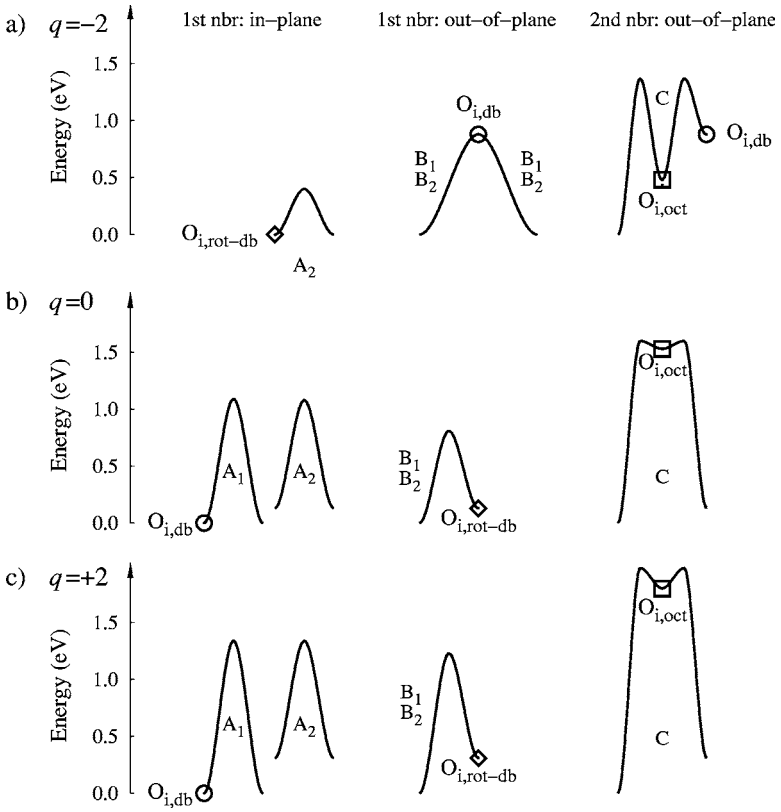

FIG. 4. Schematic of the energy surface for oxygen interstitial migration for charge states $q=-2$ (a), $q=0$ (b), and $q=+2$ (c). The zero of the energy scale corresponds to the respective ground state ($q\geq 0: O_{i,db}, q<0: O_{i,db\text{-}rot}$). Since paths B_1, B_2, and C implicitly transform between the dumbbell ($O_{i,db}$) and the rotated dumbbell ($O_{i,db\text{-}rot}$) configurations, the energetic positions of the initial and the final state differ. The energetically higher-lying state can transform into the ground state via the on-site transformation process *X* (not shown) which has a very small energetic barrier.

since the barriers for the alternative processes (A_1, A_2, B_1, and B_2) have lower barriers, they will be rate determining and the additional complexity arising for path C can be safely neglected. For the latter, we therefore considered the maximum barrier heights only (compare Table I).

In summary, a migrating oxygen atom can move through a series of single jumps with in-plane as well as out-of-plane components of the displacement vector. Since in neutral and positive charge states the migration enthalpies for in and out-of-plane paths are very similar, a near isotropic behavior would be expected. On the other hand, for the negative charge states the in-plane path A_1 is significantly lower in energy than the two lowest out-of-plane paths (B_1, B_2), which should give rise to anisotropic diffusion.

C. Comparison with experiment

Annealing measurements after electron[3,37] as well as ion irradiation[38] have shown that the onset of significant recovery occurs between 80 and 130 K which has been taken as evidence for host interstitial migration.[37] In fact, the oxygen interstitial diffusion barriers for charge states $q=-1$ and -2 are small enough to allow defect diffusion at such low temperatures. Assuming a typical annealing time of 10 min, and requiring a mean square displacement between $(100\ \mathrm{nm})^2$ and $(1000\ \mathrm{nm})^2$, we obtain threshold temperatures[39] between 80 and 100 K for charge state $q=-1$, and between 130 and 160 K for charge state $q=-2$ in good agreement with experiment. The other charge states should not contribute to annealing at temperatures less than 350 K.

Using positron annihilation spectroscopy in combination with electron irradiation of *n*-type zinc oxide samples, Tuomisto *et al.* were able to deduce an activation energy for the neutral oxygen vacancy of 1.8 ± 0.1 eV.[40] Again, the calculations are in very good agreement with this observation giving a minimum barrier of 1.87 eV for migration path A (Table I).

V. DIFFUSIVITIES

A. Derivation of diffusivities

If all migration barriers are known, the defect diffusivity is obtained by a summation over the available paths

$$D^d = \frac{1}{2}\sum_i \zeta_i \Gamma_i^d |\vec{\lambda}_i|^2, \tag{3}$$

where $|\vec{\lambda}_i|$ is the jump length, ζ_i is the multiplicity (as given in Table I), and the jump rate Γ_i^d is given by Eq. (1). By projecting the displacement vector $\vec{\lambda}_i$ onto special lattice directions the components of the diffusivity tensor can be obtained. Due to the symmetry of the wurtzite lattice, there are only two independent components, which are conventionally denoted $D_\perp$ and $D_\parallel$ for diffusion perpendicular and parallel to the $[0001]$ axis, respectively. The quasi-isotropic diffusion coefficient is given by $D=2D_\perp+D_\parallel$.

Experimentally, diffusivities are usually obtained by measuring the mobility of tracer atoms. Considering the vacancy and interstitialcy mechanisms, which have been introduced in the foregoing section, a tracer atom can only migrate if a vacancy or interstitial defect is available in its neighborhood. Therefore, the tracer diffusivity (or self-diffusion coefficient) D^* depends on the diffusivities of vacancies D^v and interstitials D^i as well as on the respective concentrations c^v and c^i according to

$$D^* = f^v Z^v c^v D^v + f^i Z^i c^i D^i, \tag{4}$$

where f^v and f^i are lattice dependent correlation factors typically of order unity, and Z^v and Z^i are the number of possible target sites. The exact determination of the correlation factors is a subject in its own right;[4] in the present work we use the approximation $f^{v,i}=1-1/Z^{v,i}$. Because the wurtzite lattice is composed of two penetrating hexagonal close packed sublattices, the coordination numbers are $Z^v=Z^i=12$. Since either interstitials or vacancies prevail under oxygen-rich and zinc-rich conditions, respectively, one of the two terms in Eq. (4) is usually dominating. Therefore, it is admissible and instructive to discuss the vacancy and interstitialcy mechanism as well as the charge states separately.

In case of an intrinsic mechanism, the defect concentrations are determined by the thermodynamic equilibrium conditions and follow an Arrhenius law behavior $c^d=c_0^d \times\exp[-\Delta G_d^f/k_BT]$, which, if entropic contributions are neglected, can be approximated by

$$c^d = c_0^d \exp[-\Delta H_d^f/k_BT], \tag{5}$$

where ΔH_d^f is the defect formation enthalpy. Therefore, in case of an intrinsic mechanism the activation energy measured in a diffusion experiment comprises both the formation (ΔH^f) and the migration enthalpy (ΔH^m). In contrast, in case of an extrinsic mechanism, the defect concentrations (c^v or c^i) are externally controlled, e.g., through intentional or unintentional doping and therefore, the activation energy represents only the migration barrier.

It is expedient to discuss the parameters which influence the tracer diffusion coefficient in the presence of an intrinsic diffusion mechanism. Apart from the obvious temperature dependence D^* is affected by (i) the chemical potential (i.e., the partial pressures of Zn and O) and (ii) the Fermi level. (i) Since the formation enthalpies in Eq. (5) depend linearly on the chemical potential,[41] according to Eq. (4) the tracer diffusion coefficient will vary as well. Neither the migration barriers ΔH_i^m nor the attempt frequencies $\Gamma_{0,i}$ are explicit functions of the chemical potential. (ii) The formation enthalpies of charged defects also change linearly with the Fermi level,[41] again affecting the tracer diffusion coefficient through Eqs. (4) and (5). In addition, the diffusion coefficient depends implicitly on the Fermi level since it determines which charge state of a given defect is the most stable, and thus which migration barrier is relevant.

In summary, in the case of an intrinsic mechanism, the dependence of the self-diffusion coefficient on the chemical potential as well as the Fermi level originates predominantly from the dependence on the defect concentration. In contrast, in the case of an extrinsic mechanism, the dependence on chemical potential and Fermi level should be significantly less pronounced.

TABLE II. Multiplicities ζ_i and displacements λ for vacancy and interstitial migration as they enter the calculation of diffusivities via Eq. (3). $\lambda_\perp$: displacement within (0001) plane in units of a; $\lambda_\parallel$: displacement parallel to [0001] axis in units of c (a and c are the lattice constants of the wurtzite structure).

Migration path	ζ_i	$\lambda_\perp$	$\lambda_\parallel$
Oxygen vacancy V_O			
1st nbr.: in-plane (A)	6	1	0
1st nbr.: out-of-plane (B)	6	$\sqrt{1/3}$	1/2
2nd nbr.: out-of-plane (C)	6	$\sqrt{4/3}$	1/2
Oxygen interstitial O_i, neutral and positive			
1st nbr.: in-plane (A_1,A_2)	6	1	0
1st nbr.: out-of-plane (B_1,B_2)	6	$\sqrt{1/3}$	1/2
2nd nbr.: out-of-plane (C)	6	$\sqrt{4/3}$	1/2
Oxygen interstitial O_i, negative charge states			
1st nbr.: in-plane (A_2)	6	1	0
1st nbr.: out-of-plane (B_1+X,B_2+X)	3	$\sqrt{1/3}$	1/2
1st nbr.: in-plane (B_1+B_1)	6	1	0
1st nbr.: out-of-plane (B_1+B_2,B_2+B_1)	6	1	1

Using Eqs. (1)–(5) and the parameters given in Table II, one arrives at the following expressions for the diffusivity tensor components for the oxygen vacancy ($\beta=1/k_BT$):

$$D_\perp = \frac{1}{2}\Gamma_0 a^2[3e^{-\beta\Delta E_A} + e^{-\beta\Delta E_B} + 4e^{-\beta\Delta E_C}],$$

$$D_\parallel = \frac{3}{4}\Gamma_0 c^2[e^{-\beta\Delta E_B} + e^{-\beta\Delta E_C}].$$

In the case of the oxygen interstitial, positive and negative charge states need to be separated. For neutral and positively charged interstitials, the energy difference (ΔE_{O_i}) between the dumbbell ($O_{i,db}$) and rotated dumbbell ($O_{i,db\text{-}rot}$) configurations is sufficiently small to assume that both types contribute to diffusion. The resulting migration paths are shown in Fig. 2; the according multiplicities and displacements are given in Table II. Taking furthermore into account the ratio of the population probabilities for the dumbbell ($O_{i,db}$) and rotated dumbbell ($O_{i,db\text{-}rot}$) states, one obtains

$$D_\perp = \frac{1}{2}\Gamma_0 a^2[3e^{-\beta\Delta E_{A1}} + 3e^{-\beta(\Delta E_{O_i}+\Delta E_{A2})} + e^{-\beta\Delta E_{B1}} + e^{-\beta\Delta E_{B2}} + 4e^{-\beta\Delta E_C}],$$

$$D_\parallel = \frac{3}{4}\Gamma_0 c^2[e^{-\beta\Delta E_{B1}} + e^{-\beta\Delta E_{B2}} + e^{-\beta\Delta E_C}].$$

On the other hand, for the negative charge states, the calculations have shown the energy difference between the two dumbbell configurations to be larger than some of the barriers in the system. Therefore, only the rotated interstitial ($O_{i,db\text{-}rot}$) can contribute to oxygen diffusion. Furthermore, the saddle point configuration along paths B_1 and B_2 is found to be essentially identical with the dumbbell interstitial

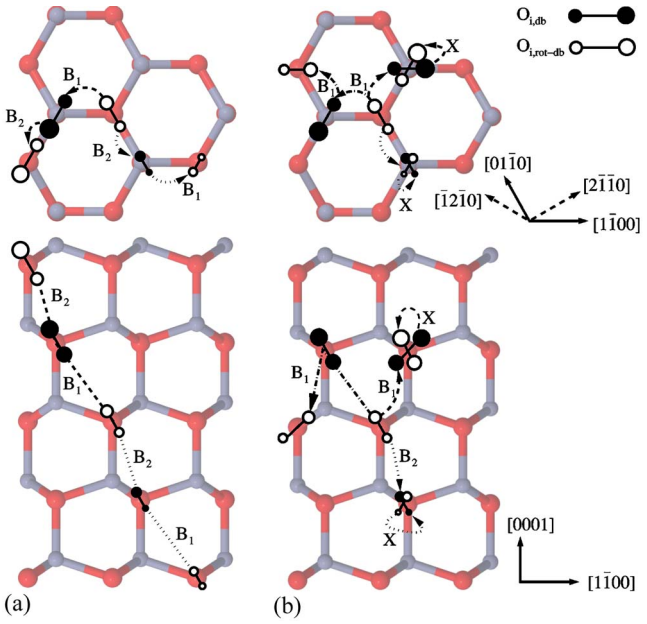

FIG. 5. (Color online) Modified migration paths for diffusion of negatively charged interstitials obtained by concatenation of the elementary paths shown in Fig. 2. (a) B_1+B_2 (dashed) and B_2+B_1 (dotted), (b) B_1+X (dashed), B_2+X (dotted), and B_1+B_1 (dash-dotted).

($O_{i,db}$). In order to account for these observations, modified first nearest neighbor migration paths need to be constructed by concatenating the elementary processes[42] B_1, B_2, and X as shown in Fig. 5. Using the multiplicities and displacements from Table II, the diffusivities are obtained as

$$D_\perp = \Gamma_0 a^2[6e^{-\beta\Delta E_{A1}} + 13e^{-\beta\Delta E_{B1}} + 7e^{-\beta\Delta E_{B2}}]$$

$$D_\parallel = \frac{27}{8}\Gamma_0 c^2[e^{-\beta\Delta E_{B1}} + e^{-\beta\Delta E_{B2}}],$$

where process C has been neglected because of its large migration barriers (see Sec. IV B and Table I). In order to obtain the tracer diffusivities (assuming purely intrinsic behavior), we used the formation enthalpies from Ref. 30 given in Table I and approximated the attempt frequency by the Debye frequency[1] which yields $\Gamma_0 \approx 8$ THz.

B. Comparison with experiment

In the past a number of accounts on the diffusion of oxygen in zinc oxide have been published (see Refs. 5–10; also compare literature review in Ref. 8). The earliest studies relied on gaseous-exchange techniques,[5,6] but later on these data have been deemed as unreliable because of experimental problems related to the use of platinum tubes[7] and the evaporation of zinc oxide.[7,8] More recent studies employed secondary ion mass spectroscopy (SIMS) to obtain diffusivities from depth profiles[8–10] and also included intentionally doped samples.[9,10] Despite these efforts a consistent picture has not emerged yet. The prefactors and activation energies reported in the literature are widely spread which according to the analysis by Tomlins *et al.*[8] is probably related to insufficient

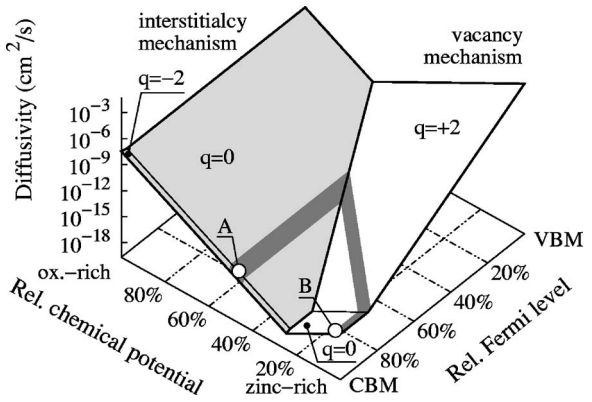

FIG. 6. Dependence of diffusivity on chemical potential and Fermi level at a temperature of 1300 K illustrating the competition between vacancy and interstitialcy mechanisms. The dark grey areas indicate the experimental data range around 1300 K. The Arrhenius plots for regions A (interstitialcy mechanism dominant) and B (vacancy mechanism dominant) are shown in Fig. 7.

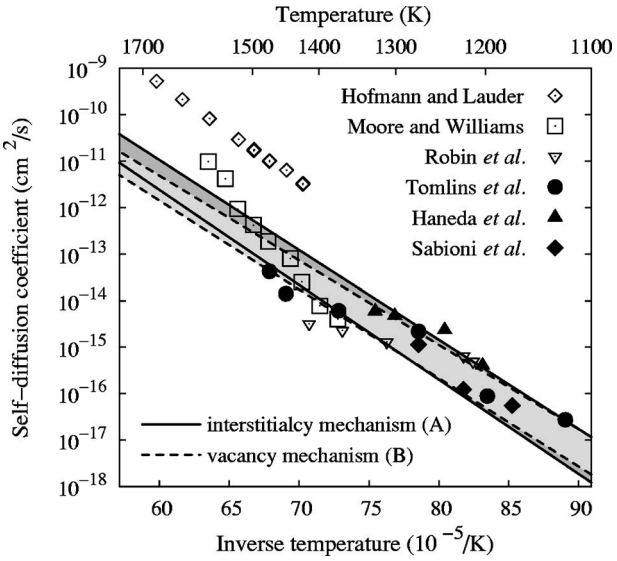

FIG. 7. Oxygen tracer diffusivity in zinc oxide from experiment and calculation. Experimental data from Moore and Williams (Ref. 5), Hofmann and Lauder (Ref. 6), Robin *et al.* (Ref. 7), Tomlins *et al.* (Ref. 8, 3M sample), Haneda *et al.* (Ref. 9), and Sabioni *et al.* (Ref. 10). Solid and dashed lines correspond to regions A (interstitialcy mechanism dominant) and B (vacancy mechanism dominant) in Fig. 6, respectively. The reliability of the data from Refs. 5 and 6 has been questioned in the past (see Refs. 7 and 8 and text for details) but included in the plot for completeness.

statistics. Direct comparison with the experimental diffusion data is further hampered, since there are unknown parameters such as the Fermi level, the chemical potentials of the constituents, or possible impurity induced changes in the intrinsic defect concentrations.

The effects of chemical potential and Fermi level as well as the resulting complicacies in the comparison with experiment are exemplified in Fig. 6. Interstitialcy and vacancy mechanisms dominate under oxygen and zinc-rich conditions, respectively. The larger formation enthalpies (ΔH^f) of oxygen interstitials as compared to vacancies are compensated by lower migration enthalpies (ΔH^m), leading to a balance between the two mechanisms. (The areas corresponding to vacancy and interstitialcy mechanisms in Fig. 6 are nearly equally large.) The transition between the two regimes is only weakly dependent on temperature showing a slight increase of the interstitialcy mechanism region with rising temperature. The range of experimental data is shown by the dark grey shaded area, which reveals that both mechanisms can *in principle* explain the experimentally observed diffusivities. Since undoped zinc oxide typically exhibits *n*-type behavior, Fig. 7 compares the temperature dependence of the diffusivity near the bottom of the conduction band for the cases A (interstitialcy mechanism dominates) and B (vacancy mechanism dominates) indicated in Fig. 6. Both mechanisms yield similar curves and show good agreement with the experimental data in the temperature region up to about 1450 K. Above this temperature the experimental data is very unreliable and subject to question as discussed before.[8]

At this point, one can conclude that both mechanisms can explain the experimentally measured diffusivities. However, since all experimental studies were performed in oxygen atmosphere, the conditions are closer to the oxygen-rich side of the phase diagram for which the interstitialcy mechanism dominates. Sabioni suggested that oxygen interstitial diffusion occurs by motion of null or negatively charged species[2] which is supported by our analysis. Zinc oxide is typically intrinsically *n*-type conducting and the oxygen interstitial is indeed found to diffuse in charge states $q=0$ and $q=-2$.

VI. CONCLUSION

We have employed density-functional theory calculations in conjunction with the climbing image nudged elastic band method to derive migration paths and saddle points for oxygen vacancy and interstitial motion in zinc oxide. Where direct comparison is possible our results agree very well with experiments. We find very low barriers for oxygen interstitials migrating in negative charge states which yields an explanation for the low onset temperatures observed in annealing experiments. The high interstitial mobility can also contribute to the radiation hardness of zinc oxide by allowing for rapid annihilation of Frenkel pairs.

Which diffusion mechanism prevails, depends on the chemical potentials of the constituents as well as the Fermi level, i.e., in practice the process conditions and the presence of impurities or dopants. Vacancy and interstitial diffusion dominate under zinc and oxygen-rich conditions, respectively. For typical diffusion experiments carried out in oxygen atmospheres, the interstitialcy mechanism is, therefore, the major path for oxygen migration.

At the time being, a direct comparison between calculation and diffusion experiments is hampered since information on chemical potentials and Fermi level is not available for the experimental data in the literature. We hope that our results will, however, serve as a motivation and support for future experiments and their interpretation. Furthermore, we anticipate that the detailed description of migration paths presented in this paper will aid the development of strategies to systematically enhance or impede the diffusion of oxygen, provide the data basis for continuum modeling of zinc oxide

structures and devices, and serve as guidance for studying atomic migration in other wurtzite crystals.

ACKNOWLEDGMENTS

We would like to thank G. Henkelman, H. Jónsson, and co-workers for kindly providing their VASP extensions (http://theory.cm.utexas.edu/henkelman) and A. Klein for helpful discussions. This project was funded by the *Sonderforschungsbereich 595* "Fatigue in functional materials" of the *Deutsche Forschungsgemeinschaft*. We also acknowledge financial support through a bilateral travel program funded by the German foreign exchange server (DAAD).

[1] U. Özgür, Y. I. Alivov, C. Liu, A. Teke, M. Reshchikov, S. Doğan, V. Avrutin, S. J. Cho, and H. Morkoç, J. Appl. Phys. **98**, 041301 (2005).
[2] A. C. S. Sabioni, Solid State Ionics **170**, 145 (2004).
[3] C. Coskun, D. C. Look, F. G. C, and S. J. R, Semicond. Sci. Technol. **19**, 752 (2004).
[4] A. R. Allnatt and A. B. Lidiard, *Atomic Transport in Solids* (Cambridge University Press, Cambridge, 2003).
[5] W. J. Moore and E. L. Williams, Discuss. Faraday Soc. **28**, 86 (1959).
[6] J. W. Hoffman and I. Lauder, Trans. Faraday Soc. **66**, 2346 (1970).
[7] R. Robin, A. R. Cooper, and A. H. Heuer, J. Appl. Phys. **44**, 3770 (1973).
[8] G. W. Tomlins, J. L. Routbort, and T. O. Mason, J. Am. Ceram. Soc. **81**, 869 (1998).
[9] H. Haneda, I. Sakaguchi, A. Watanabe, T. Ishigaki, and J. Tanaka, J. Electroceram. **4**, 41 (1999).
[10] A. C. S. Sabioni, M. J. F. Ramos, and W. B. Ferraz, Mater. Res. **6**, 173 (2003).
[11] A. F. Kohan, G. Ceder, D. Morgan, and Chris G. Van de Walle, Phys. Rev. B **61**, 15019 (2000).
[12] S. B. Zhang, S. H. Wei, and A. Zunger, Phys. Rev. B **63**, 075205 (2001).
[13] F. Oba, S. R. Nishitani, S. Isotani, H. Adachi, and I. Tanaka, J. Appl. Phys. **90**, 824 (2001).
[14] E.-C. Lee, Y.-S. Kim, Y.-G. Jin, and K. J. Chang, Phys. Rev. B **64**, 085120 (2001).
[15] S. Lany and A. Zunger, Phys. Rev. B **72**, 035215 (2005).
[16] A. Janotti and C. G. Van de Walle, Appl. Phys. Lett. **87**, 122102 (2005).
[17] P. Erhart, A. Klein, and K. Albe, Phys. Rev. B **72**, 085213 (2005).
[18] M. G. Wardle, J. P. Goss, and P. R. Briddon, Phys. Rev. B **71**, 155205 (2005).
[19] G. M. Dalpian and S.-H. Wei, Phys. Rev. B **72**, 075208 (2005).
[20] G. Henkelman, G. Jóhannesson, and H. Jónsson, in *Progress on Theoretical Chemistry and Physics* (Kluwer Academic Publishers, Dordrecht, 2000), p. 269.
[21] G. Henkelman, B. P. Uberuaga, and H. Jónsson, J. Chem. Phys. **113**, 9901 (2000).
[22] Y. Yan, S. B. Zhang, S. J. Pennycook, and S. T. Pantelides, in *Transport and Microstructural Phenomena in Oxide Electronics*, edited by D. S. Ginely *et al.*, MRS Symp. Proc. No. 666 (Materials Research Society, Warrendale, 2001), p. F2.6.
[23] G. H. Vineyard, J. Phys. Chem. Solids **3**, 121 (1957).
[24] E. Rauls and T. Frauenheim, Phys. Rev. B **69**, 155213 (2004).
[25] Rauls and Frauenheim have shown that in order to derive formation entropies of point defects very large supercells (on the order of a few hundred atoms) are needed because the entropy converges slowly with supercell size (Ref. 24). We anticipate a similar slow convergence for migration entropies and within the present approach, supercells which are sufficiently large for this purpose are computationally too expensive. The entropic contributions are, therefore, expected to be small and have been neglected in the present work.
[26] G. Kresse and J. Furthmüller, Phys. Rev. B **54**, 11169 (1996).
[27] P. E. Blöchl, Phys. Rev. B **50**, 17953 (1994); G. Kresse and D. Joubert, Phys. Rev. B **59**, 1758 (1999).
[28] J. P. Perdew, in *Electronic Structure of Solids*, edited by P. Ziesche and H. Eschrig (Akademie Verlag, Berlin, 1991).
[29] S. L. Dudarev, G. A. Botton, S. Y. Savrasov, C. J. Humphreys, and A. P. Sutton, Phys. Rev. B **57**, 1505 (1998).
[30] P. Erhart, K. Albe, and A. Klein (unpublished).
[31] F. Birch, J. Geophys. Res. **83**, 1257 (1978).
[32] A. Every and A. McCurdy, *Landolt-Börnstein: Numerical Data and Functional Relationships in Science and Technology, New Series*, Vol. III/29A (Springer, Heidelberg, 1992).
[33] The implementations of the climbing image nudged elastic band and the dimer method for VASP were obtained from http://theory.cm.utexas.edu/henkelman.
[34] G. Henkelman and H. Jónsson, J. Chem. Phys. **111**, 7010 (1999).
[35] S. B. Zhang, S.-H. Wei, and A. Zunger, Phys. Rev. Lett. **84**, 1232 (2000).
[36] G. Makov and M. C. Payne, Phys. Rev. B **51**, 4014 (1995).
[37] Y. V. Gorelkinskii and G. D. Watkins, Phys. Rev. B **69**, 115212 (2004).
[38] K. Lorenz, E. Alves, E. Wendler, O. Bilani, W. Wesch, and M. Hayes, Appl. Phys. Lett. **87**, 191904 (2005).
[39] In order for a defect to anneal it must be able to migrate a certain distance $\sqrt{\langle r^2\rangle_{\min}}$ during the annealing time, τ. Using the Einstein relation $\langle r^2\rangle = 6D\tau$, the onset temperature for annealing is established as the temperature for which $6D\tau$ exceeds $\sqrt{\langle r^2\rangle_{\min}}$.
[40] F. Tuomisto, K. Saarinen, D. C. Look, and G. C. Farlow, Phys. Rev. B **72**, 085206 (2005).
[41] S. B. Zhang and J. E. Northrup, Phys. Rev. Lett. **67**, 2339 (1991).
[42] Since in negative charge states the barriers for the second nearest neighbor path C are at least 30% larger than any of the first neighbor paths, it is not considered in the following.